Design of a Low Threshold Single-Mode In-P Laser Using Regrowth-Free Fabrication

A. Sharma , *Member, IEEE*, P. Landais , *Senior Member, IEEE*, M. Srivastava , M. Wallace, F. Smyth , A. Kaszubowska-Anandarajah , *Senior Member, IEEE*, and P. Anandarajah , *Senior Member, IEEE*

Abstract—We describe the design procedure, optimization, and fabrication cycle of an index-pattern FP laser on an InP platform. The design parameters of the ridge and reflector (based on slots) are extracted through simulations. In addition, the performance of reflectors with varying slot widths is analyzed. Subsequently, the extracted parameters are used in a rate equation model to predict the performance of the laser in terms of its $L-I$ characteristics and the sidemode suppression ratio (SMSR). Moreover, the simulated results are compared with the experimental characterization of lasers fabricated with estimated design parameters revealing that the index-pattern laser with 0.3 μm slot width delivers the best performance by demonstrating a threshold current of $\sim$30 mA and SMSR $>$ 30 dB.

Index Terms—Single mode laser, Fabry-Perot resonators, Integrated optoelectronics, Phase noise, RIN.

I. INTRODUCTION

SINGLE mode semiconductor lasers, such as distributed feed-back (DFB) and distributed Bragg reflector (DBR) lasers, are known for their low threshold [1] and a high sidemode suppression ratio (SMSR) [2]. These positive attributes lead to the employment of such lasers in diverse applications including optical communications, sensing [3], and high-resolution spectroscopy [4]. However, the fabrication of DFB and DBR lasers requires precise lithography and etching [5] increasing the cost and reducing the yield. Single mode index-pattern Fabry-Perot (IP FP) lasers can be a viable replacement for DFB or DBR

lasers offering simplified fabrication and photonic integration [6], [7], [8]**.** The benefit of such lasers is that they can be realized using low-resolution photolithography and requires a few fabrication steps [9]. This in turn leads to significantly lower costs. Typically, the structure of index-patterned lasers consists of a gain section followed by a reflector section, which is fabricated by etching slots on the ridge waveguide. Periodically etched slots on the surface of the optical waveguide, where the period between the slot is maintained according to the Bragg wavelength [10]**,** provides wavelength-specific reflection and creates lasing of a single longitudinal mode. Such lasers exhibit similar characteristics to DFB and DBR devices including a low linewidth and high SMSR [11]. Furthermore, they support regrowth-free fabrication, offering merits such as minimized fabrication cycle, shortened development time, and reduced cost [12], [13], [14], [15], [16]. In the past decade or two, there have been many demonstrations of slotted lasers exhibiting low threshold currents and high SMSR. For example, a surface grating single mode laser featuring a threshold current of 20 mA, an optical linewidth of 210 kHz, and an SMSR of 50 dB was demonstrated in [17]. Another sub-micron slot-based FP laser portraying a 22 mA threshold current, 43 dB SMSR and wavelength tunability of 38 nm was reported in [18]. While the work published to date explains the design of the slot reflectors and their optimization, to the best of our knowledge, none of these reports incorporated detailed simulation results matched with experimental outcomes.

In this paper, we describe the step-by-step procedure for the design and optimization of a single mode IP FP laser. We first use an open-source software "modesolver.py" [19] to determine the optimum width of the ridge. Subsequently, using the CAvity Modelling Framework [20] software, we focus on the design parameters of the slot reflectors that determine the threshold current, sidemode suppression ratio, and linewidth of such lasers. In these simulations, the effect of the slot width and depth on the reflection coefficients is studied. Then, we extract the reflectance band of the slot grating for varying slot widths and the net modal gain from the material used for the laser fabrication. Once the required parameters are determined, they are used in a rate equation model to verify the performance of the laser, using the slot width as the control parameter. Finally, we carry out experimental characterization on the fabricated InP FP lasers with different slot widths and use them to validate the results obtained from the rate equation simulation model.
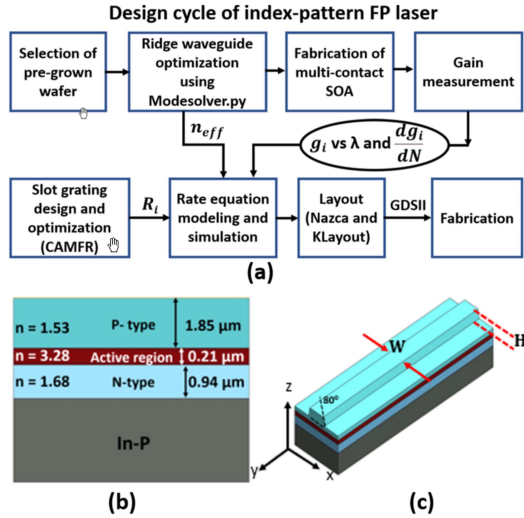
Fig. 1. (a) Flow chart for designing an index-pattern FP laser, (b) layer stack of wafer, and (c) 3-dimentional structure of the ridge laser.

This paper is organized in the following manner: Section II deals with simulation of the ridge waveguide and the slot reflectors, and the subsequent extraction of the reflection characteristics with respect to the slot width. Section III describes the experimental estimation of the gain spectrum of the gain section of the device, which is then fed to the laser rate equation model to obtain the laser characteristics, as discussed in Section IV. The experimental characterisation of the fabricated devices is detailed in Section V. In addition, we measure the linewidth variation as a function of the slot width. Finally, the findings are concluded in Section VI.

II. DESIGN AND OPTIMIZATION

In this section, we describe a complete procedure of the design and optimization process of an IP FP laser using the flow chart shown in Fig. 1(a). A standard wafer grown on an InP substrate, exhibiting a peak wavelength at 1545 nm, is selected. The wafer contains a five quantum well active layer sandwiched by a p-doped AlGaInAs layer (at the top) and an n-type AlGaInAs layer (at the bottom), as shown in Fig. 1(b). The effective refractive indices of the p-type, active region and n-type layers are 1.53, 3.28, and 1.68, respectively. Such an arrangement of a high refractive index layer in between two layers of low refractive indices ensures optical confinement of the laser emission field along the z-axis as depicted in Fig. 1(c). A ridge structure on the top p-layer confines the optical mode in the horizontal direction (the x-axis).

The width of the ridge plays an important role in maximizing the coupling of optical power into a single mode fibre. Hence, the mode field distribution pattern is calculated for various ridge widths, to determine the dimension suitable for fabrication. A Python-based open-source simulation tool, known as modesolver.py, is used for this purpose, and an optimum ridge width and effective refractive index (n_{eff}) is obtained for the best confinement of the optical field in the waveguide. The software uses finite difference eigenmode solver (FDE) that determines

the spatial profile and frequency dependence of modes within a waveguide. This involves solving Maxwell's equations on a cross-sectional mesh representing the waveguide. The solver computes essential parameters such as mode field profiles, effective index, and loss.

After determining the width of the waveguide, the reflectors are realized by etching a pattern of slots on the ridge. The reflection coefficients and reflectance bands are extracted for various slot widths using another open-source simulation platform (CAMFR). CAMFR computes frequency-domain eigenmode expansion techniques that calculate reflectivity, transmittivity, and loss of shallow/deep multiple slot structure. These estimations are critical for the design of the laser and will be discussed in detail in later sections.

A. Ridge Waveguide

A shallow etched ridge waveguide, fabricated on the top layer by an etching process, results in optical confinement in the horizontal direction (x-direction). Fig. 1(c) depicts a ridge structure of width W, where the material is removed along z-direction up to a depth of H by etching. The width (W) and etch depth (H) must be optimised to allow coupling of the fundamental mode between the active layer and the ridge, while suppressing the higher order spatial modes. The reason for minimizing the intensity of the higher-order modes in the waveguide is to minimize the coupling losses to single mode fiber and reduce the threshold for the fundamental mode that contributes to lasing. For optimization of W and H, the 2-dimensional (2-D) full vectorial algorithm solving a Laplace equation (modesolver.py) is employed [21], [22]. The solver returns the transverse optical modes with their respective E-field distribution on the cross-sectional area of the waveguide. The ridge waveguide structure is constructed by defining the thickness of layers, refractive index profile, W and H. For the shallow etch ridge waveguide, the value of H is chosen as 1.35 μm [23] because it is the maximum allowed etch depth for the chosen wafer. However, the optimization of W can be performed for any suitable value of H. The angle of the side walls of the ridge is defined as 80º (as shown in Fig. 2) to account for fabrication errors.

The optimization of the ridge width is carried out by performing the simulation for various values of W. While the solver provides the solution for all the modes supported in the waveguide, we consider only the first three transverse electric modes (TE_{00}, TE_{10}, and TE_{20}) for the optimization process. This is because a significant amount of the total optical power ($\sim$95%) is contained in these modes. Fig. 3(a)–(d) shows the plots of the power distribution pattern ($|E|^2$) for the first three TE modes for three different values of ridge width. In the case of W = 4 μm, the higher order modes, TE_{10} and TE_{20}, are seen to be coupled into the ridge waveguide. The power of TE_{10} and TE_{20} modes coupled to the waveguide decreases as W is reduced to 2 μm. Hence, the modes TE_{10} and TE_{20} do not contribute to the lasing due to the low coupled power. In addition, the power of TE_{10} and TE_{20} coupled into the ridge is suppressed further for W = 1 μm. However, the coupled power of the fundamental mode also reduces, as can be seen in Fig. 3(e)–(h). The primary
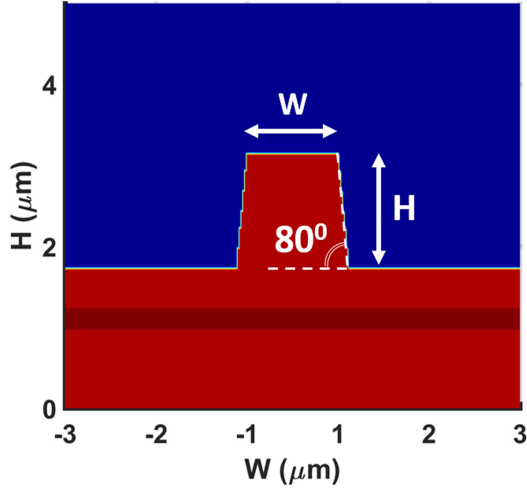
Fig. 2.   Cross-sectional view of ridge structure.

reason for the reduction in the coupled power is the leakage of the electric field outside the ridge waveguide due to scattering loss. As shown Fig. 3(g), the power of the TE_{00} mode coupled into the ridge is highest in the case of W = 2 μm, while the higher order modes are suppressed. Hence, a 2 μm wide ridge is chosen for design and fabrication.

B. Slot Reflectors

The performance of the reflector section (slot grating) is studied, as the next step. The slot grating is implemented by periodically etching slots on the ridge waveguide, as shown in Fig. 4. These slots create a discontinuity in the refractive index that causes wavelength-specific reflections of the electromagnetic wave, and therefore contribute to the wavelength selectivity of the resonant modes in the laser cavity. The reflection coefficient of the grating depends on the geometry (slot width and depth) and the number of slots. In addition, the wavelength selectivity is controlled by the spatial period between the slots and can be determined by Bragg's equation given in (1).

$$\Lambda = \frac{k \cdot \lambda_{Bragg}}{2 \cdot n_{eff}}. \tag{1}$$

Where Λ, k, λ_{Bragg}, n_{eff} are the grating period, period order, Bragg peak wavelength, and effective refractive index of the grating respectively. n_{eff} of the un-etched, etched, and grating section are obtained from the simulation discussed in the previous section and is calculated to be 3.183, 3.190, and 3.189, respectively. Several methods have been proposed to simulate the performance of slot reflectors [24], [25], [26], [27], [28], [29], [30]. In this paper, we use the open-source CAMFR to carry out the analysis and estimate the behaviour of the slot reflectors.

The grating is realised as a 1-D slot structure created by defining the thickness of the layers (p-type, active region, and n-type), slot width (S_w) and slot spacing (S_s) (as shown in Fig. 4), and period Λ defined as $\Lambda = S_w + S_s$. The period of the slot grating, calculated by setting the grating order at k = 42, λ_{Bragg} = 1545 nm (as the spectral peak of the material is at 1545 nm), results in a value of $\sim$10.17 μm. The period

order of 42 provides a 36.8 nm free spectral range, which leads to Bragg wavelengths of 1508.2 nm and 1581.8 nm. The net modal gain at 1508.2 nm and 1581.8 nm are much lower than 1545 nm and does not contribute in lasing. Thereafter, the reflection and transmission coefficients are extracted for 8, 10, and 12 cascaded slots by varying S_w while keeping the period constant. Fig. 5(a) shows the dependence of the reflection coefficient on S_w and S_d (slot depth) for a different number of slots. The plot reveals that the reflectivity increases with an increase in S_w, S_d, and the number of slots. Fig. 5(a) clearly shows that a high reflection coefficient is obtained for the values $S_w = 0.3$ μm and $S_d = 1.35$ μm. It should be noted here that the maximum possible value of S_d is equal to the etch depth of the ridge waveguide (H), which is 1.35 μm.

As the next step, we examine the dependence of the reflection coefficient on the operational wavelength. Here again using CAMFR, we extracted the reflection coefficients for a wavelength range of 1.5 μm to 1.6 μm (at a resolution of 0.1 μm). For this simulation, $S_d = 1.35$ μm (maximum etch depth) and S_w is varied between 0.2 μm and 1.4 μm. The value of Λ is kept unchanged throughout the simulation. Fig. 5(b) shows the reflectance band for various values of S_w. The plot reveals the presence of three reflectance bands at the Bragg peaks for each value of the slot width. Moreover, 0.3 μm and 0.7 μm slot widths give the highest and lowest reflectivity at the lasing wavelength of 1545 nm, respectively. For the fixed period order, the 0.3 μm slot attains $\sim$40% reflectivity at an operating wavelength of 1545 nm. We attribute the poor performance of the 0.7 μm slot to the high scattering loss at the Bragg wavelength.

III. Gain Measurement

The gain section of the laser is essentially a semiconductor optical amplifier (SOA), with its performance metrics such as L − I characteristics, optical spectrum, etc., relying on the gain parameters of the material. Moreover, the dependence of gain on injection current is critical to predict the characteristics of the laser. The net gain (g) provided by the SOA is a combination of the gain caused by the stimulated emission of photons and optical loss caused by material defects. Additionally, the injection of carriers into the gain medium alters the refractive index of the medium, which has an impact on the spectral characteristics of the gain media. Hence, it is important to establish a correspondence between the injected current and the gain spectrum of the SOA. In this section, we describe the procedure for extracting the dependence of gain characteristics on the carrier density and wavelength, which in turn is dependent on the injected current.

Several methods have been proposed to measure the gain parameter of the material used in the SOA, such as the optical transmission method [31], Hakki − Paoli method of analysis of amplified spontaneous emission (ASE) spectrum [32], [33], [34], [35], [36], comparison of ASE spectrum of distinct length SOAs [37], and segmented SOAs [38]. The method described in [32], [33], [34], [35], [36], [37], shows limited accuracy in gain measurements due to the requirement of a high-resolution optical spectrum analyser (OSA) and poor optical coupling. The method proposed in [38] is an improved method for the
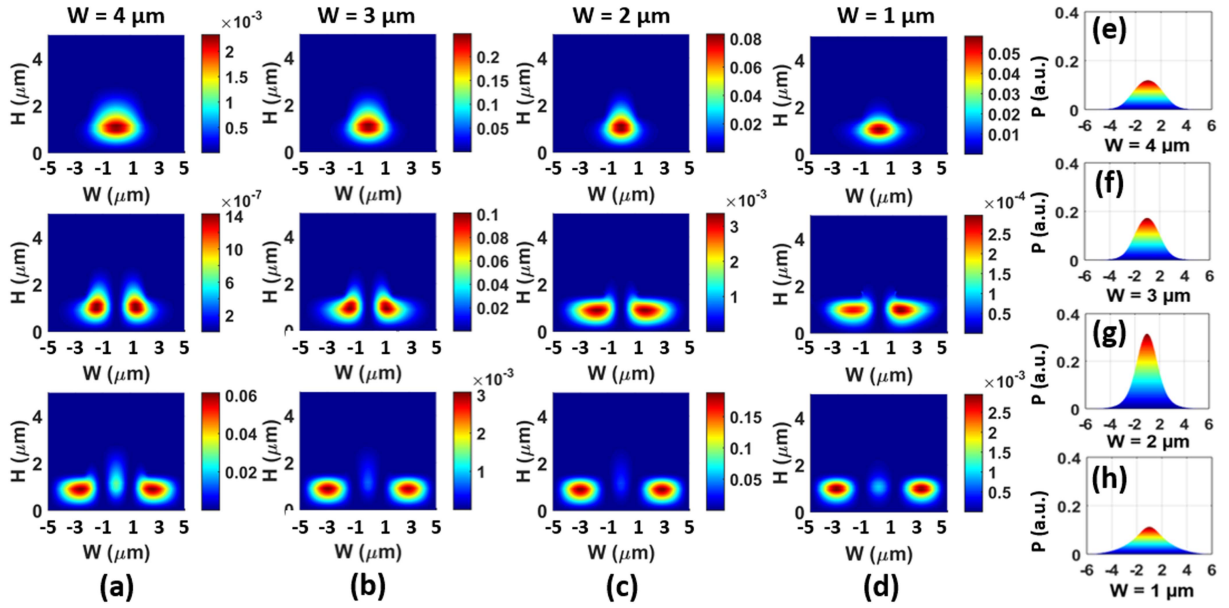
Fig. 3. Power distribution patterns in TE$_{00}$, TE$_{10}$, and TE$_{20}$ modes for (a) $W = 4\,\mu$m, (b) $W = 3\,\mu$m, (c) $W = 2\,\mu$m, and (d) $W = 1\,\mu$m, respectively, and the beam profile (arbitrary unit) of the TE$_{00}$ mode for the varying ridge widths (e) $W = 4\,\mu$m, (f) $W = 3\,\mu$m, (g) $W = 2\,\mu$m, and (h) $W = 1\,\mu$m.
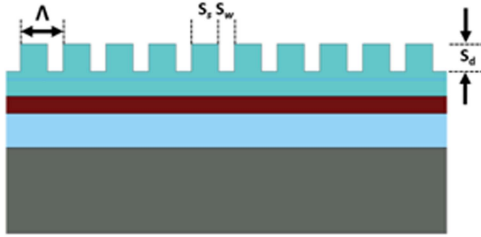

Fig. 4. Schematic of the design of slot reflectors. Here: Λ is the grating period, S$_w$ is slot width, and S$_s$ is slot spacing.

gain measurement that overcomes the mentioned drawbacks. Hence, we used the multi-section SOA method by comparing ASE spectra taken at various injection currents and extracting the gain profile at distinct values of carrier density.

The effective carrier density (N) that contributes to spontaneous emission in an SOA can be calculated by finding the roots of (2) for N at various supplied currents (I). Later, the obtained N is used to calculate the differential gain of the SOA.

$$C \cdot N^3 + B \cdot N^2 + A \cdot N - \frac{\eta \cdot I}{e \cdot V} = 0 \qquad (2)$$

Where, C, B A, η, I, q, V are the Auger coefficient, bi-molecular coefficient, nonradiative recombination coefficient, current injection efficiency, current, electronic charge, and the volume of active region respectively.

The net modal gain $g(\lambda)$, which is a function of wavelength, can be extracted from the measurement of the ASE spectrum by using (3).

$$P_{ASE}\ (\lambda) = \eta_c \frac{p_{sp}\,(\lambda)}{g\,(\lambda)} \left(e^{g(\lambda) \cdot L} - 1 \right) \qquad (3)$$

where $P_{ASE}(\lambda)$ and $p_{sp}(\lambda)$ are the total output optical power from an SOA of length L and spontaneous emission power per

unit length at wavelength λ respectively, η_c is the output power coupling efficiency, and L is the length of the gain section. $P_{ASE}(\lambda)$ is measured for two SOA sections of different lengths L_1 and L_2 driven by the same value of current, which can be expressed using (3) as

$$P_{ASE}^{L_1}\ (\lambda) = \eta_c \frac{p_{sp}\,(\lambda)}{g\,(\lambda)} \left(e^{g(\lambda) \cdot L_1} - 1 \right) \qquad (4)$$

$$P_{ASE}^{L_2}\ (\lambda) = \eta_c \frac{p_{sp}\,(\lambda)}{g\,(\lambda)} \left(e^{g(\lambda) \cdot L_2} - 1 \right) \qquad (5)$$

Where $P_{ASE}^{L1}(\lambda)$ and $P_{ASE}^{L2}(\lambda)$ are the output optical power of an SOA of length L$_1$ and L$_2$. Taking the ratio of (4) and (5), and rearranging, we get (6).

$$\frac{\left(e^{g(\lambda) \cdot L_1} - 1 \right)}{\left(e^{g(\lambda) \cdot L_2} - 1 \right)} - \frac{P_{ASE}^{L_1}\,(\lambda)}{P_{ASE}^{L_2}\,(\lambda)} = 0 \qquad (6)$$

Hence, $g(\lambda)$ can be determined from (6) by finding the roots of the equation.

We used an integrated two-section SOA (gain section) with lengths $\sim$244 μm (SOA$_1$) and $\sim$200 μm (SOA$_2$). Electrical isolation is maintained between gain sections to restrict the flow of current between them. Initially, we confirm the presence of the ASE by placing an infrared card in front of the output facet biasing the front section (SOA$_1$) at 25 mA. Then, optical power from the output facet of the device is coupled into a lensed fibre with the help of an auto-aligner for maximizing the coupled power and maintaining the alignment. The current applied to SOA$_1$ is swept from 1 mA to 175 mA and an optical spectrum ($P_{ASE}^{L_1}(\lambda)$) is recorded for each value. Next, the current input to the sections SOA$_1$ and SOA$_2$ are tied together, and the current is swept again from 1 to 175 mA, while measuring the optical spectrum ($P_{ASE}^{L_2}(\lambda)$). Thereafter, the values of the net modal gain are extracted using (6) by substituting L$_1$ = 244 μm
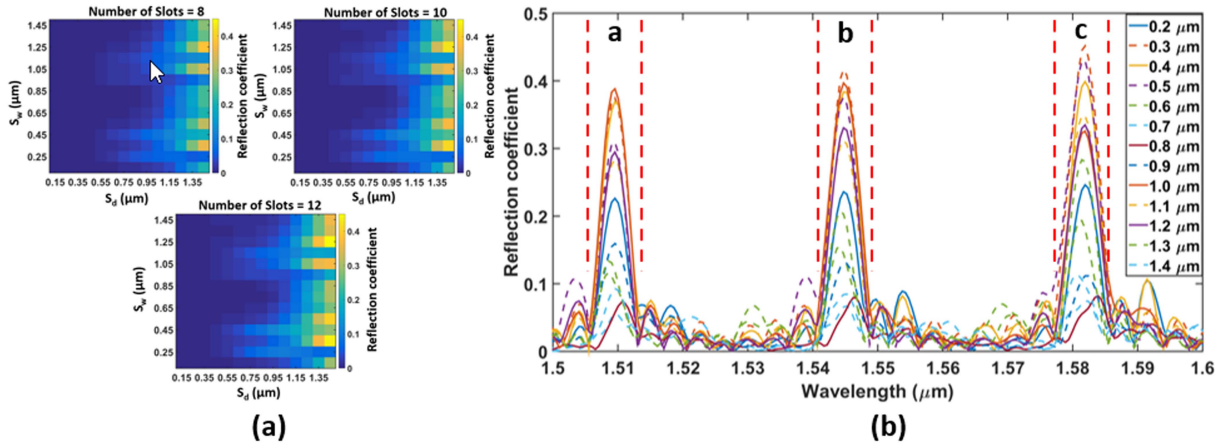
Fig. 5. Plot of the (a) variation of the reflection coefficient with respect to slot width and slot depth for various numbers of slots and (b) trend of reflection coefficient with respect to wavelength for different values of slot width.
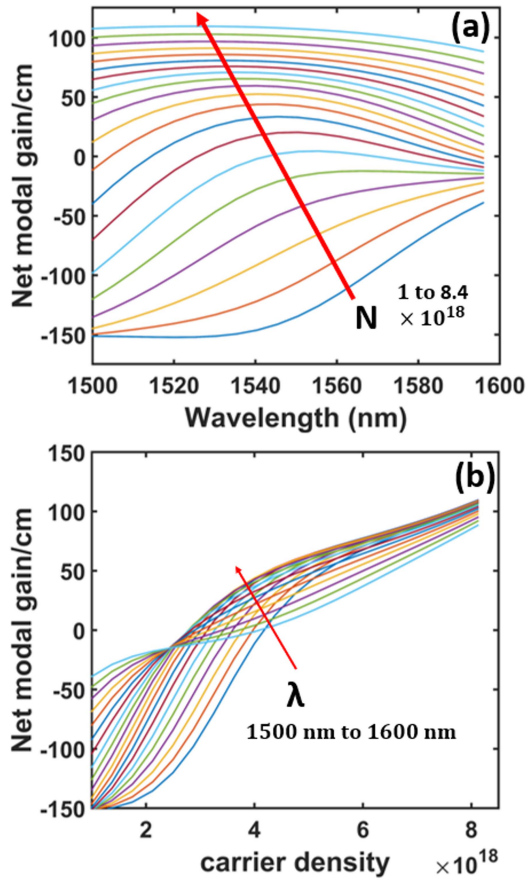

Fig. 6. Plots of (a) net modal gain vs wavelength and (b) net modal gain vs current density.
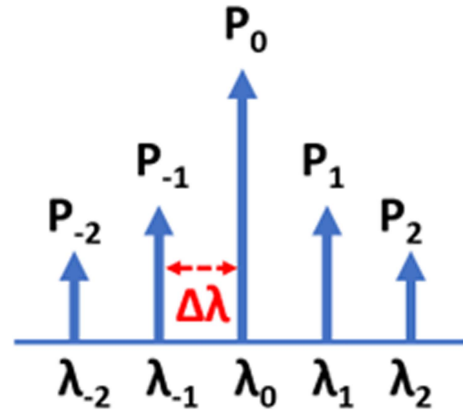

Fig. 7. Pictorial representation of the laser spectrum with five longitudinal modes.

density for a wavelength ranging between 1500 nm and 1600 nm. Thus, a relationship between the carrier density and the gain spectrum of the medium is established, which is essential for implementing the rate equation model of the laser, as discussed in the next section.

IV. RATE EQUATION MODEL

The performance of the laser can be simulated using the rate equations, where a set of three differential equations represents the time variation of the carrier density (N) and photon density (P_i). The P_i is the density of photons of the ith longitudinal mode. The (8) and (9) show the laser rate equation for the five modes where P_0 is central mode and, P_{-2}, P_{-1}, P_1, P_2, are side modes as shown in Fig. 7. The spacing between the longitudinal modes with respect to central wavelength (λ_o) is dependent on the length of the gain section and can be determined by (7).

$$\Delta\lambda = \frac{\lambda_o{}^2}{2 \cdot n_{eff} \cdot L} \tag{7}$$

The calculated wavelengths of the longitudinal modes in a 380 μm long laser, with the central mode at 1545.0 nm, are

and $L_2 = (244 + 200)$ μm, and the respective $P_{ASE}(\lambda)$ for all values of carrier densities. The range of currents used for this measurement corresponds to the carrier density values ranging from 1×10^{18} cm^{-3} to 8.42×10^{18} cm^{-3}. Fig. 6(a) shows the net modal gain as a function of wavelength (ranging from 1500 nm to 1600 nm) for different carrier densities. Similarly, Fig. 6(b) represents the net modal gain as a function of carrier

1543.03 nm, 1544.01 nm, 1545.98 nm, 1546.96 nm, respectively. As discussed in Section II-B, the reflection coefficient depends on the wavelength of operation. Hence, the reflection coefficients (R_i) are extracted from the reflectance band (shown in Fig. 5(b)). Subsequently, the differential gain of each longitudinal mode (P_0, P_{-2}, P_{-1}, P_1, and P_2,) is extracted from the plot shown Fig. 6(b) and used in the rate equation model.

$$\frac{dN}{dt} = \frac{I}{e \cdot V} - \sum_{i=-2}^{2} G_i(N) \cdot (N - N_0)$$

$$\cdot \frac{P_i}{1 + \epsilon \cdot P_t} - N_k + F_N \tag{8}$$

$$\frac{dP_i}{dt} = \Gamma \cdot G_i(N) \cdot (N - N_0) \cdot \frac{P_i}{1 + \epsilon \cdot P_t}$$

$$- \frac{P_i}{\tau_{p_i}} + \Gamma \cdot \beta_{sp} + F_{p_i} \tag{9}$$

$$\tau_{pi} = \frac{1}{v_g} \left(\alpha_i + \frac{1}{2 \cdot L} \cdot \ln \frac{1}{R_1 \cdot R_i} \right)^{-1} \tag{10}$$

$$N_k = A \cdot N + B \cdot N^2 + C \cdot N^3 \tag{11}$$

$$G_i(N') = v_g \left. \frac{dg_i}{dN} \right|_{N=N'} \tag{12}$$

$$D_{pp_i} = \Gamma \cdot \beta_{sp} \cdot B \cdot N^2 \cdot P_i \tag{13}$$

$$D_{nn_i} = \frac{D_{pp_i}}{\Gamma} + \frac{N_k}{V} \tag{14}$$

$$F_N = \sqrt{\sum_{i=-2}^{2} \frac{2 \cdot D_{nn_i}}{t_s}} \tag{15}$$

$$F_{p_i} = \sqrt{\frac{2 \cdot D_{pp_i}}{t_s}} \tag{16}$$

F_N, F_{P_i}, are the Langevin noise source for carrier density, photon density, and phase of N, P_i, and, respectively, and are calculated using (13) and (14) [39], [40]. The set of ordinary differential (8) and (9) is solved using the Runge-Kutta numerical technique and parameters mentioned in Table I. The N_k, G_i, and P_t are carrier recombination rate calculated using (11), the net modal gain using (12) and total photon number, respectively. τ_{p_i} is the photon lifetime that depends on the length of cavity, reflectance of both mirrors, internal loss, and group velocity. τ_{p_i} can be calculated by using (10). The value of $\alpha_h = 2$ is used in the simulation as in [41]. Only five modes are considered in the simulation to study the static behaviour such as L-I, threshold and SMSR of the laser. The reason for considering only five modes is to analyse the effect of the reflectance band b as presented in Fig. 5(b) on the suppression of sidemodes. The longitudinal modes lying outside of pass band b are not considered. The modes under the passbands a and c attain low gain (approximately $\frac{0}{cm}$ at 30 mA as depicted in Fig. 6(a)), hence does not contribute to lasing. Moreover, the longitudinal modes which are outside of passbands a, b, and c are suppressed due to low reflectivity ($R < 0.1$). The simulation is carried out by using values of R_i for various slot widths and values obtained from (13)–(16). In addition, the value of $\frac{dg_i}{dN}$

TABLE I
PARAMETERS AND VALUES USED IN THE SIMULATION

| Symbol	Parameter	Value
N_0	Threshold carrier density	2.08×10^{18} /cm^3
L	Length of the laser	380 μm
w	Width of ridge waveguide	2×10^{-4} cm
d	Thickness of active region	0.03×10^{-4} cm
I	Current	30 mA
e	Electronic charge	1.6×10^{-19} C
n_{eff}	Effective refractive index	~3.19
v_g	Group velocity	9.39×10^7 m/s
G_i	Net modal gain calculated from Fig. 6	
ϵ	Gain compression factor	5×10^{-17} cm^3
Γ	Confinement factor	0.05
C	Auger constant	3.5×10^{-29} cm^6/s
B	Bimolecular recombination coefficient	1×10^{-10} cm^6/s
A	Non radiative recombination coefficient	0.1×10^9
η	Injection efficiency	0.8
β_{sp}	Spontaneous emission factor	3.2×10^{-5}
α_h	Linewidth enhancement factor	2
t_s	Sampling time	5 ns
α_i	Internal loss	40 /cm
R_1	Reflection coefficient of back facet	0.95
R_i	Reflection coefficient of grating	-
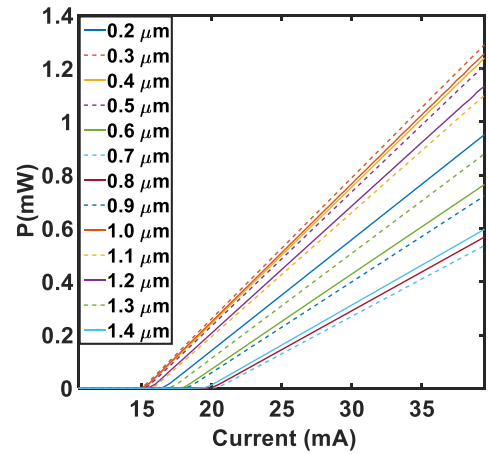
Fig. 8. Simulated $L - I$ plot of IP FP for the slot width varying from 0.2 μm to 1.4 μm.

(differential gain for i^{th} mode) is obtained by calculating the slopes from the net modal gain versus carrier density presented in Fig. 6(b) for all five longitudinal modes at carrier density $= 4.27 \times 10^{18}$/cm (bias above threshold). The calculated $\frac{dg_i}{dN}$ for the modes λ_0, λ_1, λ_{-1}, λ_2, and λ_{-2} are 2.13×10^{-17}, 2.11×10^{-17}, 2.10×10^{-17}, 2.08×10^{-17}, and 2.07×10^{-17} respectively. Initially, the simulation is performed to analyse the effect of the slot width on $L - I$ characteristics by calculating the output power with respect to the supplied current. Fig. 8 shows the $L - I$ data obtained from the simulation. It reveals that the threshold of the laser for each of the slot widths lies between 15 mA to 21 mA, with the 0.3 μm, 0.4 μm, 1.0 μm wide slots achieve the lowest and the 1.4 μm, 0.7 μm, and 0.8 μm wide slots the highest thresholds. Only the 0.3 μm wide slot is considered for further simulation since it exhibits the lowest threshold.

In the next simulation, we compare the SMSR performance of the IP FP laser and a conventional FP laser using the rate
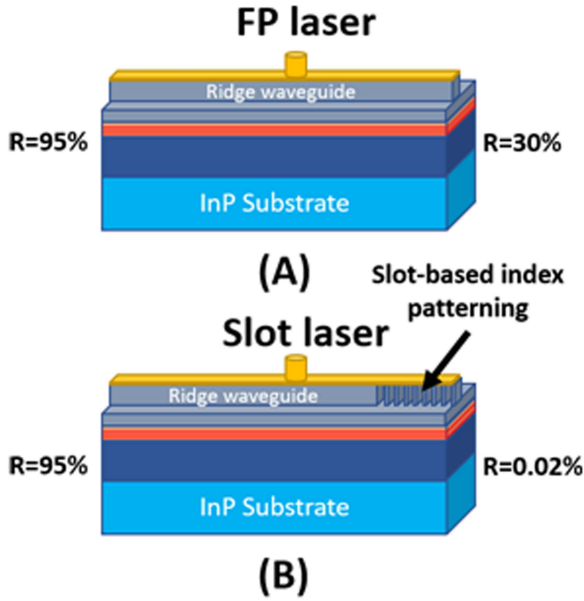
Fig. 9. Schematic of the (a) structure of a conventional FP and (b) an IP FP. Here: R is the reflectivity.
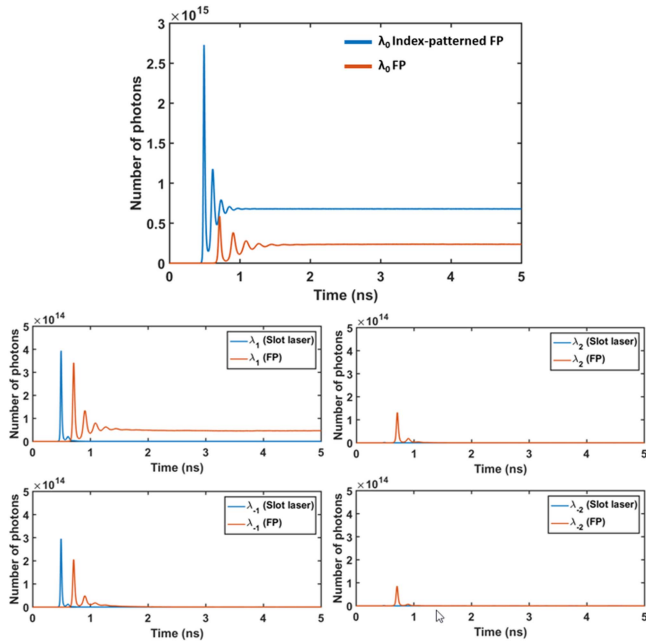

Fig. 10. Comparison of the number of photons vs. time for five modes of an IP FP (blue) and a conventional FP laser (orange) biased at 30 mA.

equation model and extracting the time variation of the photon density for each longitudinal mode. The architectures of an FP and IP FP are shown in Fig. 9. The FP structure is defined by L = 380 μm, $R_1 = 0.95$ (HR coated back facet) and $R_2 = 0.33$ (front facet). Similarly, the structure of IP FP keeps the same length and R_1 as for FP. However, the IP FP used slotted grating of $S_w = 0.3$ μm, which makes R_2 wavelength dependent, as shown in Fig. 5(b). Fig. 10 represents the comparison of the time trace of the emitted photon density obtained from the simulation for five modes of the FP and the IP FP. The simulation reveals that the photon density in steady state for the λ_0 mode is ∼2.8
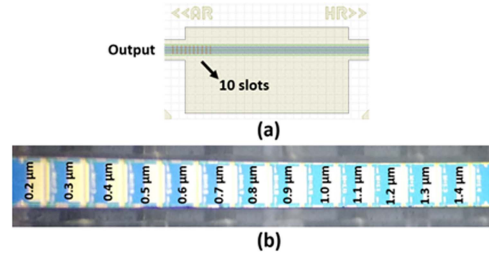

(a)

(b)

Fig. 11. Layout of the IP FP, HR: high reflective coating, AR: Antireflective coating, and (b) Picture of fabricated lasers on a bar of varying slot width.

higher in the case of the indexed-patterned FP than that of the conventional FP. In addition, we see a 3.4×10^2, 4.7, 8.1, 5.6 times reduction in the number of photons in λ_1, λ_{-1}, λ_2, and λ_{-2} modes for the IP FP compared to the conventional FP. The reason for the higher photon density in the central mode is the suppression of the side mode. From the simulations, the SMSR is calculated by taking the logarithm of the ratio of the steady-state number of photons lying in the central mode and sidemodes. The simulation returns SMSR values of ∼7.1 dB and ∼37 dB for the conventional FP and the IP FP lasers, respectively, showing a notable improvement in SMSR provided by the IP FP.

So, in conclusion, the simulation shows that the 0.3 μm slot achieves lowest threshold and best slope efficiency among all variants. The main reason for the low threshold of 0.3 μm slot laser is high reflectivity and low transmission loss at a wavelength of 1545 nm. In addition, 0.3 μm slot laser attains SMSR > 36 dB for 30 mA supply current.

V. EXPERIMENTAL CHARACTERIZATION

The IP FPs with varying slot widths were designed using the Nazca design software [42]. An example of the layout of an IP FP is shown Fig. 11(a). As highlighted earlier, the IP FPs are fabricated using a regrowth free technique [6]. A photograph of the fabricated lasers on a cleaved bar is shown in Fig. 11(b). The back and front facets of the laser are highly reflective and antireflective coated, respectively. To initiate the characterization, the laser bar is mounted on a subcarrier printed circuit board (PCB) and a DC current is supplied to the contact pads of the laser by using DC current probes. To obtain the L-I curve of the laser, the applied current is swept from 0 to 100 mA and the output optical power is measured using a wide area photodetector with a responsivity of 0.95 A/W. The measurements are carried out on 6 bars and for 13 different slots widths, varying between 0.2 μm and 1.4 μm.

Fig. 12 shows the L − I plot of IP FP lasers from one of the bars. The data shows that, as in the case of the simulations, the laser with a 0.3 μm slot width exhibits the lowest threshold of ∼16 mA. On the other hand, the 0.9 μm and 1.1 μm slot width lasers show the highest threshold. Further investigation is carried out on all the variants of IP FP laser by measuring the optical spectrum and extracting the SMSR. To measure the optical spectrum, the optical power from the output facet of the laser is coupled into a lens-ended fibre and fed to an optical spectrum analyser (OSA). The laser current is swept from 0 to
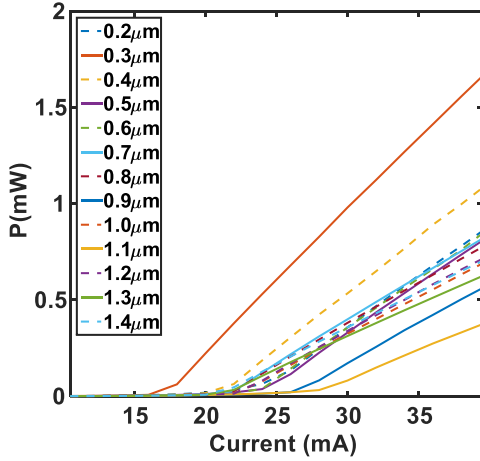
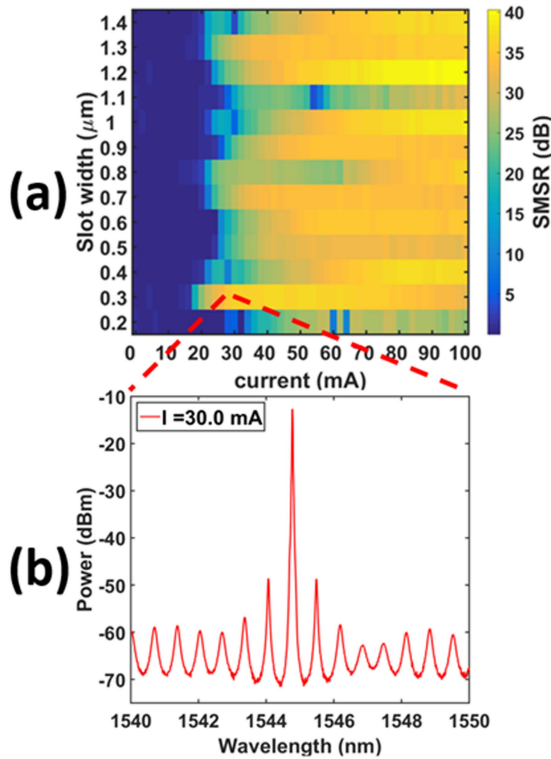Fig. 12. Plot of measured L−I data of IP FPs for varying slot width from 0.2 μm to 1.4 μm.

Fig. 13. (a) SMSR plot for laser with varying slot width and (b) optical spectrum of the IP FP with a slot width of 0.3 μm biased at 30 mA.
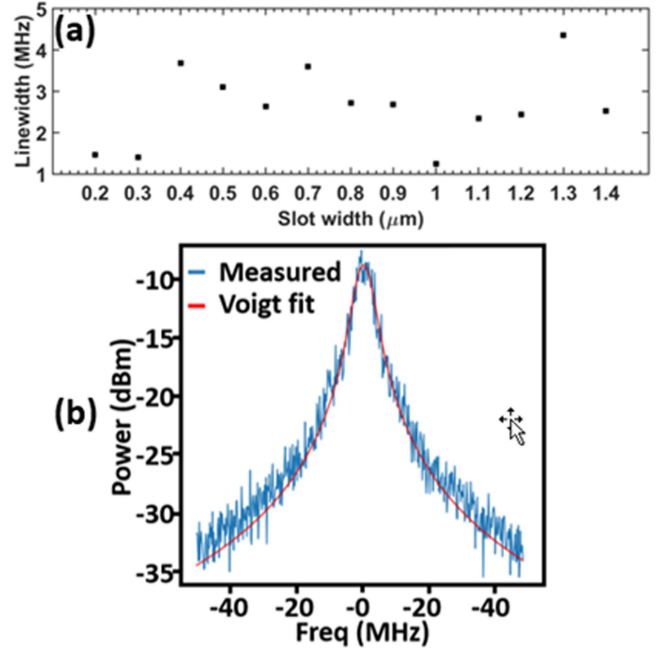

Fig. 14. (a) Linewidth measurements of IP FPs for slot width varying from 0.2 μm to 1.4 μm and (b) measured and Voigt fit of RF beat spectrum.

100 mA at a resolution of 0.2 mA and the SMSR is measured. The results, plotted in Fig. 13(a), show that the IP FP with a slot width of 0.3 μm, attains an SMSR greater than 30 dB for bias currents higher than 24 mA. An example of the optical spectrum for 0.3 μm IP FP biased at 30 mA and featuring SMSR > 35 dB is shown in Fig. 13(b).

Next, we compare the threshold currents and SMSR values obtained from the simulation and experimental results. Firstly, both the simulation and the experimental characterization show that 0.3 μm slot laser exhibits the lowest threshold at ∼15 mA and ∼16 mA, respectively. Also, the laser with the 0.3 μm slot

attains an SMSR of ∼36 dB and ∼37 dB in the simulation and experimental characterization, respectively. The small difference in the simulated and measured threshold is due to inaccuracies in the gain measurement.

Finally, the linewidth of each variant of the IP FP laser is determined using the delayed self-heterodyne method [43]. For the linewidth measurement all laser variants are biased at current of 65 mA. The results, displayed in Fig. 14(a), show that all the variants exhibit linewidths between 1 and 5 MHz, with the lowest linewidth of ∼1 MHz attained when the slot widths are 0.3 μm and 1.0 μm. Fig. 14(b) shows the linewidth of 0.3 μm slot laser determined by Voigt profile fitting of measured RF beat spectrum. Such low linewidth performance (in both simulation and experimental results) can also be linked to the low threshold, high SMSR and high slope efficiency.

VI. CONCLUSION

We describe a step-by-step procedure for designing and optimizing a low threshold laser using open-source software and a rate equation model. The simulation on the optimization of the ridge width using modesolver.py software reveals that the fundamental mode attains maximum power coupled into the 2 μm wide and 1.35 μm thick ridge at a wavelength of 1545 nm. Subsequently, the characteristics of the reflector such as the reflectivity and reflectance band are determined using CAMFR software. The simulation shows that the slots with a width of 0.3 μm and a depth of 1.35 μm exhibit the highest reflectivity. Thereafter, the performance of all the variants of IP FP laser is evaluated by simulations that employ the rate equation model. The final validation is carried out via experimental characterization. We see an excellent agreement between the simulation and experimental characterization. The 0.3 μm IP FP shows best

performance in terms of low threshold and linewidth, and high SMSR.

The results obtained from simulation and experimental characterization on optimized design parameters of slot-based IP FP laser could help design and fabricate a high-performance, low-cost laser for employment in optical communication systems.

REFERENCES

[1] S. Tsuji, A. Ohishi, H. Nakamura, M. Hirao, N. Chinone, and H. Matsumura, "Low threshold operation of 1.5-μm DFB laser diodes," *J. Lightw. Technol.*, vol. 5, no. 6, pp. 822–826, Jun. 1987, doi: 10.1109/JLT.1987.1075569.

[2] R. M. Lammert, J. S. Hughes, S. D. Roh, M. L. Osowski, A. M. Jones, and J. J. Coleman, "Low-threshold narrow-linewidth InGaAs-GaAs ridge-waveguide DBR lasers with first-order surface gratings," *IEEE Photon. Technol. Lett.*, vol. 9, no. 2, pp. 149–151, Feb. 1997, doi: 10.1109/68.553068.

[3] A. Larsson, "Advances in VCSELs for communication and sensing," *IEEE J. Sel. Top. Quantum Electron.*, vol. 17, no. 6, pp. 1552–1567, Nov./Dec. 2011, doi: 10.1109/JSTQE.2011.2119469.

[4] A. Bawamia et al., "Semiconductor laser modules for precision spectroscopy applications in space," in *Proc. SPIE*, vol. 11180, pp. 1936–1944, 2019, doi: 10.1117/12.2536111.

[5] C. H. Lin, Z. H. Zhu, Y. Qian, and Y. H. Lo, "Cascade self-induced holography: A new grating fabrication technology for DFB/DBR lasers and WDM laser arrays," *IEEE J. Quantum Electron.*, vol. 32, no. 10, pp. 1752–1759, Oct. 1996, doi: 10.1109/3.538781.

[6] Q. Lu et al., "Single mode lasers based on slots suitable for photonic integration," *Opt. Exp.*, vol. 19, no. 26, pp. B140–B145, Dec. 2011, doi: 10.1364/OE.19.00B140.

[7] W.-H. Guo et al., "Integrable slotted single-mode lasers," *IEEE Photon. Technol. Lett.*, vol. 24, no. 8, pp. 634–636, Apr. 2012, doi: 10.1109/LPT.2012.2184745.

[8] A. Abdullaev et al., "Linewidth characterization of integrable slotted single-mode lasers," *IEEE Photon. Technol. Lett.*, vol. 26, no. 22, pp. 2225–2228, Nov. 2014, doi: 10.1109/LPT.2014.2350772.

[9] P. Ma et al., "30-Gbps directly modulated semiconductor lasers based on surface high-order gratings," *IEEE Photon. Technol. Lett.*, vol. 33, no. 4, pp. 197–200, Feb. 2021, doi: 10.1109/LPT.2021.3049859.

[10] Q. Lu, W. -H. Guo, D. Byrne, and J. F. Donegan, "Design of slotted single-mode lasers suitable for photonic integration," *IEEE Photon. Technol. Lett.*, vol. 22, no. 11, pp. 787–789, Jun. 2010.

[11] B. Kelly et al., "Discrete mode laser diodes with very narrow linewidth emission," *Electron. Lett.*, vol. 43, no. 23, pp. 1282–1284, Nov. 2007.

[12] N. P. Kelly et al., "Regrowth-free single mode laser based on dual port multimode interference reflector," *IEEE Photon. Technol. Lett.*, vol. 29, no. 3, pp. 279–282, Feb. 2017, doi: 10.1109/LPT.2016.2637565.

[13] P. E. Morrissey, N. Kelly, M. Dernaika, L. Caro, H. Yang, and F. H. Peters, "Coupled cavity single-mode laser based on regrowth-free integrated MMI reflectors," *IEEE Photon. Technol. Lett.*, vol. 28, no. 12, pp. 1313–1316, Jun. 2016, doi: 10.1109/LPT.2016.2541695.

[14] V. Tolstikhin, "Distributed feedback lasers for regrowth-free multi-guide vertical integration in InP," in *Proc. IEEE 23rd Annu. Meeting Photon. Soc.*, 2010, pp. 521–522, doi: 10.1109/PHOTONICS.2010.5698990.

[15] L. Caro, M. Dernaika, N. P. Kelly, P. E. Morrissey, J. K. Alexander, and F. H. Peters, "An integration-friendly regrowth-free tunable laser," *IEEE Photon. Technol. Lett.*, vol. 30, no. 3, pp. 270–272, Feb. 2018, doi: 10.1109/LPT.2017.2781799.

[16] R. M. Briggs et al., "Regrowth-free single-mode quantum cascade lasers with power consumption below 1 W," *Appl. Phys. Lett.*, vol. 105, no. 14, Oct. 2014, Art. no. 141117, doi: 10.1063/1.4898003.

[17] K. Dridi et al., "Low-threshold and narrow linewidth two-electrode MQW laterally coupled distributed feedback lasers at 1550 nm," in *Proc. 38th Eur. Conf. Exhib. Opt. Commun.*, 2012, pp. 1–3, doi: 10.1364/ECEOC.2012.Mo.1.E.4.

[18] T. Yu et al., "Single-mode and wavelength tunable lasers based on deep-submicron slots fabricated by standard UV-lithography," *Opt. Exp.*, vol. 20, no. 15, Jul. 2012, Art. no. 16291, doi: 10.1364/OE.20.016291.

[19] Apr. 13, 2024. [Online]. Available: https://github.com/jtambasco/modesolverpy

[20] Apr. 15, 2024. [Online]. Available: https://camfr.sourceforge.net/

[21] J. Xiao et al., "Full-vectorial mode solver for anisotropic optical waveguides using multidomain spectral collocation method," *Opt. Commun.*, vol. 283, no. 14, pp. 2835–2840, 2010.

[22] A. B. Fallahkhair, K. S. Li, and T. E. Murphy, "Vector finite difference modesolver for anisotropic dielectric waveguides," *J. Lightw. Technol.*, vol. 26, no. 11, pp. 1423–1431, Jun. 2008.

[23] P. Ma et al., "Single-mode semiconductor lasers fabricated by standard photolithography for direct modulation," *Opt. Exp.*, vol. 27, no. 4, Feb. 2019, Art. no. 5502, doi: 10.1364/OE.27.005502.

[24] H. Wenzel, R. Guther, A. M. Shams-Zadeh-Amiri, and P. Bienstman, "A comparative study of higher order Bragg gratings: Coupled-mode theory versus mode expansion modeling," *IEEE J. Quantum Electron.*, vol. 42, no. 1, pp. 64–70, Jan. 2006, doi: 10.1109/JQE.2005.859910.

[25] S. O'Brien et al., "Design, characterization, and applications of index-patterned Fabry–Pérot Lasers," *IEEE J. Sel. Top. Quantum Electron.*, vol. 17, no. 6, pp. 1621–1631, Nov./Dec. 2011, doi: 10.1109/JSTQE.2011.2118192.

[26] H. Kogelnik et al., "Coupled-wave theory of distributed feedback lasers," *J. Appl. Phys.*, vol. 43, no. 5, pp. 2327–2335, 1972.

[27] Q. Y. Lu et al., "Analysis of slot characteristics in slotted single-mode semiconductor lasers using the 2-D scattering matrix method," *IEEE Photon. Technol. Lett.*, vol. 18, no. 24, pp. 2605–2607, Dec. 2006.

[28] P. Bienstman et al., "Optical modelling of photonic crystals and VCSELs using eigenmode expansion and perfectly matched layers," *Opt. Quantum Electron.*, vol. 33, no. 4, pp. 327–341, 2001.

[29] M. G. Moharam et al., "Rigorous coupled-wave analysis of planar-grating diffraction," *JOSA*, vol. 71, no. 7, pp. 811–818, 1981.

[30] W. Sun, Q. Lu, W. Guo, M. Wallace, F. Bello, and J. F. Donegan, "Analysis of high-order slotted surface gratings by the 2-D finite-difference time-domain method," *J. Lightw. Technol.*, vol. 35, no. 1, pp. 96–102, Jan. 2017, doi: 10.1109/JLT.2016.2627604.

[31] C. Ellmers et al., "Measurement and calculation of gain spectra for (GaIn)As/(AlGa)As single quantum well lasers," *Appl. Phys. Lett.*, vol. 72, no. 13, pp. 1647–1649, Mar. 1998, doi: 10.1063/1.121140.

[32] B. W. Hakki et al., "cw degradation at 300 K of GaAs double-heterostructure junction lasers. II. Electronic gain," *J. Appl. Phys.*, vol. 44, no. 9, pp. 4113–4119, 1973.

[33] H. Wang and D. T. Cassidy, "Gain measurements of Fabry-Pe/spl acute/rot semiconductor lasers using a nonlinear least-squares fitting method," *IEEE J. Quantum Electron.*, vol. 41, no. 4, pp. 532–540, Apr. 2005.

[34] D. Hofstetter and J. Faist, "Measurement of semiconductor laser gain and dispersion curves utilizing fourier transforms of the emission spectra," *IEEE Photon. Technol. Lett.*, vol. 11, no. 11, pp. 1372–1374, Nov. 1999.

[35] W.-H. Guo, Y.-Z. Huang, C.-L. Han, and L.-J. Yu, "Measurement of gain spectrum for Fabry-Perot semiconductor lasers by the Fourier transform method with a deconvolution process," *IEEE J. Quantum Electron.*, vol. 39, no. 6, pp. 716–721, Jun. 2003.

[36] W.-H. Guo, Q.-Y. Lu, Y.-Z. Huang, and L.-J. Yu, "Fourier series expansion method for gain measurement from amplified spontaneous emission spectra of Fabry-Perot semiconductor lasers," *IEEE J. Quantum Electron.*, vol. 40, no. 2, pp. 123–129, Feb. 2004.

[37] A. Oster et al., "Gain spectra measurements by a variable stripe length method with current injection," *Electron. Lett.*, vol. 33, no. 10, pp. 864–866, 1997.

[38] D. Pustakhod, K. Williams, and X. Leijtens, "Fast and robust method for measuring semiconductor optical amplifier gain," *IEEE J. Sel. Top. Quantum Electron.*, vol. 24, no. 1, Jan./Feb. 2018, Art. no. 3100309, doi: 10.1109/JSTQE.2017.2737581.

[39] G. L. Lippi et al., "Analytical vs. Numerical Langevin description of noise in small lasers," Mar. 21, 2019. Accessed: Jan. 9, 2023. [Online]. Available: https://arxiv.org/pdf/1903.08859.pdf

[40] L. A. Coldren et al., *Diode Lasers and Photonic Integrated Circuits*. Hoboken, NJ, USA: Wiley, 2012.

[41] G. Feng et al., "Simulation and analysis of single mode semiconductor laser," [Online]. Available: https://scholar.google.com/scholar?hl=en&as_sdt=0%2C5&q=Simulation+and+Analysis+of+Single+Mode+Semiconductor+Laser+Guangjian+Feng+and+Xavier+Fernando+&btnG=

[42] "Homepage," Nazca design. Nov. 22, 2017. Accessed: Jun. 18, 2023. [Online]. Available: https://nazca-design.org/

[43] M. Chen et al., "Ultra-narrow linewidth measurement based on Voigt profile fitting," *Opt. Exp.*, vol. 23, no. 5, pp. 6803–6808, Mar. 2015, doi: 10.1364/OE.23.006803.